



Flexible kirigami with local cylindrical shell design for stretchable microstrip antenna



Ji Zhang ^{a,b}, Lamei Zhang ^c, Yafei Wang ^d, Youshan Wang ^{a,b}, Changguo Wang ^{a,b,*}

^a National Key Laboratory of Science and Technology on Advanced Composites in Special Environments, Harbin Institute of Technology, Harbin 150080, People's Republic of China

^b Center for Composite Materials and Structures, Harbin Institute of Technology, Harbin 150001, People's Republic of China

^c Department of Information Engineering, Harbin Institute of Technology, Harbin 150001, People's Republic of China

^d Department of Aeronautics and Astronautics, Fudan University, Shanghai 200433, People's Republic of China

ARTICLE INFO

Keywords:

Kirigami
Cylindrical shell
Snap-Through Instability
Stretchable Microstrip Antenna

ABSTRACT

This paper proposes a flexible kirigami structure. It has rotating rigid squares and cylindrical shells to improve the flexibility of the structure and produce snap-through instability. First, a mechanical spring model based on a quarter of unit cell was established to predict the mechanical characteristics of its deployment. The elastic deformation energy stored in the mechanical system was calculated, and the applied force was obtained after deriving the displacement. By assuming that the rotational stiffness of the spring is related to the length, elastic modulus, and thickness of the cylindrical shell, the coefficients used to quantify the stiffness of the rotational spring were obtained through a finite element calculation and the mechanical characteristics of the structure were obtained. The accuracy was verified through experiments and the finite element method. Then, the deployment mechanism and parameterization of the structure were analyzed. The snap-through characteristics of the cylindrical shell were analyzed, and the curvature of the second steady state was obtained using the minimum potential energy. The influence of the geometric parameters of the unit cell, such as its length, thickness, and the center angle of the cylindrical shell, on the snap-through instability was analyzed. By stretching or compressing it at different positions, different mechanical characteristics of the deployment were obtained. Finally, based on the designed structure, a stretchable microstrip antenna was designed to achieve high gain while the center frequency remained fixed. An antenna was fabricated and measured, and the test results are in good agreement with the simulated results. This work may provide theoretical guidance for the design and application of deformable structures.

1. Introduction

Kirigami, the creative art of paper cutting and folding, and the tessellations derived from the resulting shapes have recently emerged as prototypical routes for fabricating a new class of mechanical metamaterials [1–6]. The source material can be conveniently cut when flat and then transformed into complex 3D configurations upon stretching by exploiting local elastic instabilities [7–14]. Kirigami shapes consisting of square unit cells can have a negative Poisson's ratio and provide a route for forming complex 3D structures [15–19]. Such a unit cell is cut from a paper square without folds and is manually stretched until it arrives at a maximum opening angle. It is then in a maximally stretched state that cannot be further stretched or rotated due to its infinite

stiffness, beyond which the hinge will break [20,21]. Although significant progress has been achieved, there are still some scientific challenges that need to be addressed in the development of kirigami structures with thick panels, since continuous external energy is required to preserve the structural configuration [22–26]. Therefore, cylindrical shell is often placed at the hinge position to improve the stiffness of the structure and obtain snap-through characteristics [27,28]. Due to its unique deformable characteristics, such as twisting and rotation, the structure described in this paper has a rich set of mechanical properties, such as tensile strength, toughness, stiffness [29,30].

Moreover, the development of deformable stealth aircraft has attracted much attention [31,32]. Metasurfaces have significant

* Corresponding author.

E-mail address: wangcg@hit.edu.cn (C. Wang).

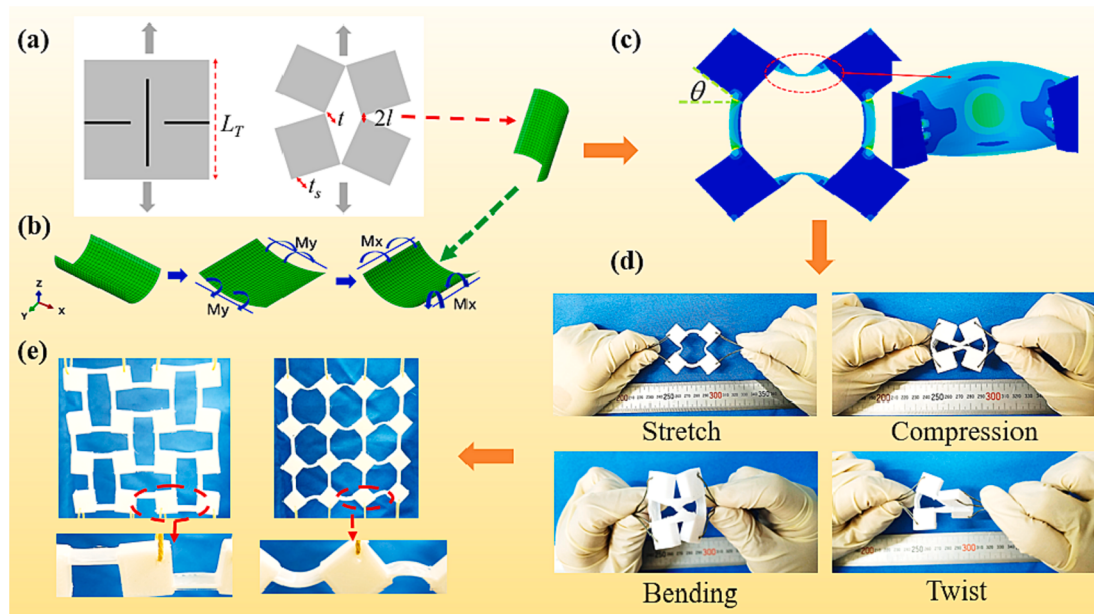


Fig. 1. (a) Folding and deployable rigid squares. (b) Cylindrical shell. (c) Flexible kirigami unit cell. (d) Demonstration of stretching, compressing, bending, and twisting. (e) Flexible kirigami structure formed from an array of four unit cells.

potential for wavefront manipulation, and their fabrication is less complex [33,34]. However, structural modification is generally challenging once the metamaterials or metasurfaces have been fabricated, rendering them functionally nonreconfigurable. Reconfigurable metamaterials could be designed to achieve dynamic control over some physical properties, allowing one metadevice to realize multiple functions [35–38]. Kirigami, by making cuts in a thin sheet, can be employed to design highly stretchable and morphable mechanical metamaterials [39–42].

The rest of this paper is organized as follows. First, a flexible kirigami structure is presented. Then, a theoretical model is developed to predict the deployable behavior and snap-through mechanism. Third, the deployment mechanism and parameterization of the structure are analyzed. Finally, a stretchable microstrip antenna is designed to achieve high gain while the center frequency remains the same. This paper provides reference for the development of kirigami structure and its application in stretchable microstrip antenna.

2. Design strategy

The unit cell of a kirigami structure is composed of square plates. Each square plates can undergo rotational motion, which can lead to a negative Poisson's ratio. However, since the second stable state of the unit cell is always generated when square plate is rotated to nearly 90°, it is difficult to control the snap-through instability of the structure. For this kind of kirigami structure, previous studies have assumed a rigid body at the crease and lacked mechanical degrees of freedom. The cylindrical shell has a high relative energy, the stable large deformation sustaining load capacity, easy to prepare, the buffer impact load, the energy absorption, and vibration isolation, and so on. The cylindrical shell has a series of characteristics such as excellent mechanical properties, lightweight, high strength, and has a wide range of application prospects in smart deformation, energy collection, bionic and other fields. By adding a cylindrical shell to the local "hinge", more degrees of freedom are introduced, increasing the bending stiffness at the crease. Through the partial cylindrical shell design, the curvature is introduced, which greatly expands the design space of the kirigami structure and greatly increases the overall flexibility. A flexible kirigami structure is proposed, as shown in Fig. 1. The unit cell of the flexible kirigami structure is a combination of square plates and cylindrical shells that

have a stable configuration when they bent through some angle. When the unit cell is subjected to tension in the vertical direction, the four square plates rotate and the four interconnecting ligaments between each plate, which are the cylindrical shells, become bent. The cylindrical shells are arranged so that they can always bend in the direction of greater bending moment to make the snap-through phenomenon more obvious.

The geometric parameters of the unit cell are shown in Fig. 1(c). The total length is \$L_T\$. The thickness of a square is \$t_s\$. The length of a cylindrical shell is \$2l\$, and its thickness is \$t\$. The angle between a square plate and the horizontal is defined as the deployment angle, denoted by \$\theta\$.

The unit cell can be stretched, compressed, bent, or twisted, and has multiple deformation modes, as shown in Fig. 1(d). The demonstration shows that the structure can undergo various deformations without breaking. An array of unit cells constitute a flexible kirigami structure, as is shown in Fig. 1(e).

3. Nonlinear spring model

A mechanical spring model consisting of a quarter of a unit cell was developed, as shown in Fig. 2(a). The model consists of a rigid square plate and two rotational springs. The size of the square plate is \$L_s \times L_s\$. The constraints on points B and C are controlled by three movable supports (boundary conditions). Point B can rotate and move horizontally but cannot move vertically. Similarly, point C can rotate and move vertically but cannot move horizontally. The vertical force \$F_y\$ is applied at point A so that the rigid square rotates clockwise. The inclination angle of AB is denoted by \$\theta\$, which represents the rotation of the plate. The vertical displacement of point A is \$V\$. The angle \$\theta\$ is limited between 0 and \$\pi/2\$ during the rotation [22].

As shown in Fig. 2(b), the cylindrical shells have length \$2l = 13\$ mm, diameter \$R_1 = 6\$ mm, thickness \$t = 0.6\$ mm, and central angle \$\beta = 180^\circ\$. During bending of the cylindrical shell, the bending moment initially increases almost linearly until it reaches a maximum. Then, the bending moment instantly becomes smaller and tends to stabilize. The extreme value of the snap-through bending moment of the opposite-sense bending is greater than that of the equal-sense bending. The snap-through phenomenon is more obvious in opposite-sense bending. For deformation cloud diagram, the red indicates the maximum stress, and the blue indicates the minimum stress. The intermediate portion of the

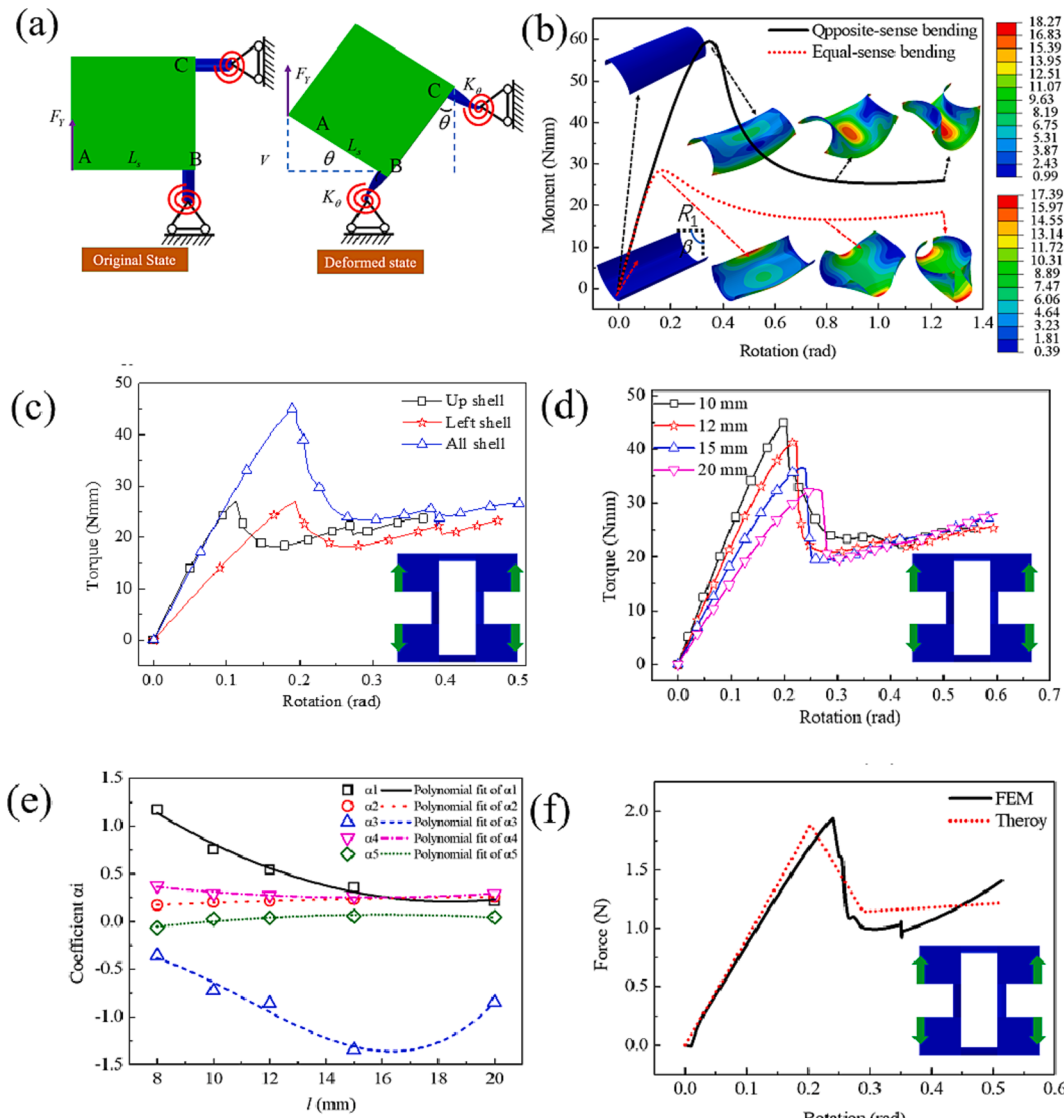


Fig. 2. (a) Mechanical spring model representing a quarter of the unit cell. (b) Moment vs. rotation curves of a cylindrical shell. (c) Moment vs. rotation curves of cylindrical shells in different positions. (d) Moment vs. rotation curves of cylindrical shells with different lengths (10,12,15,20 mm). (e) Polynomial fit coefficients α_i ($i = 1, \dots, 5$) vs. length. (f) Force vs. rotation curves in deployment.

cylindrical shell is the largest, and the edge is minimal. The stress in the opposite-sense bending intermediate part is greater than the stress of the equal-sense bending intermediate part.

Fig. 2(c) compares moment vs. rotation curves of cylindrical shells at different positions by finite element method (FEM). The interaction between rigid squares and cylindrical shells uses shell-to-solid coupling constraints, adding contact between components. The model is meshed, and rigid square uses a C3D8R unit, which features: 8-node linear brick, reduced integration, hourglass control, and the cylindrical shell is: 4-node doubly curved thin or thick shell, reduced integration, hourglass control, finite membrane strains. The snap-through instability intervals of the left and upper cylindrical shells relative to the angle θ are different. The snap-through curve of the structure is a non-linear superposition of the two. If the length, thickness, etc. of the cylindrical shell are reasonable, then snap-through can be realized at any angle.

The elastic deformation energy stored in the mechanical system is.

$$W = K_\theta \theta^2 \quad (1)$$

where $\theta = \arcsin(V/L_s)$. The deformation energy W is a function of the vertical displacement V . The vertical force F_Y conjugated to V can then

be obtained as.

$$F_Y = \frac{dW}{dV} = \frac{2K_\theta \theta}{L_s \cos \theta} \quad (2)$$

FEM was used to simulate moment M vs. angle θ responses for various sizes of cylindrical shell, as shown in Fig. 2(d). The linear slopes correspond to the rotational stiffness K_θ . As the length increased, the stiffness gradually decreased.

To apply the mechanical spring model to the unit cell, we need to quantify the stiffness of the rotational spring K_θ in terms of the geometrical parameters l , L_s , and b , and the material parameters (i.e., Young's modulus E and Poisson's ratio ν). We need to simulate one interconnect cylindrical shell to evaluate K_θ . The moment M at the square plate is applied and the rotation of the square plates is denoted by the inclined angle θ . K_θ is closely related to half of cylindrical shell size l . Through dimensional analysis, K_θ can be assumed to have the following form:

$$K_\theta = \alpha_i E b l, \quad i = 1, 3, 5 \quad (3)$$

where $E = 60$ MPa is Young's modulus, b is the out-of-plane thickness,

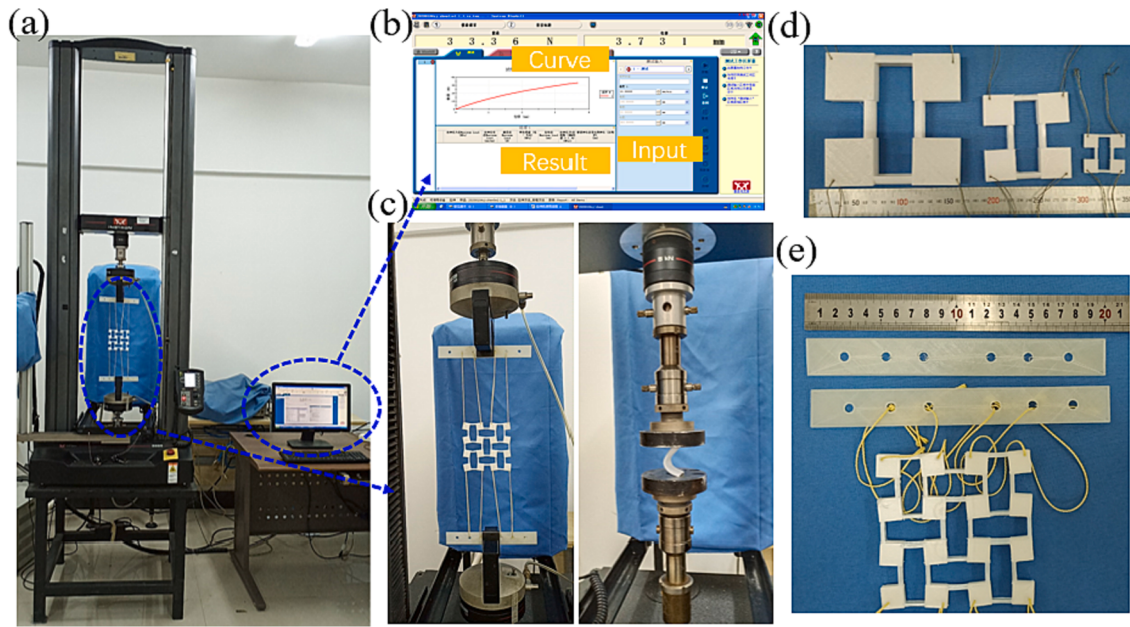


Fig. 3. Test rig and specimens: (a) Test rig. (b) Bluehill monitor. (c) Testing a specimen. (d) Unit cells of designed structure. (e) Designed structure and platens with holes.

and α_i is a dimensionless coefficient to be determined. As shown in Fig. 2(e), the coefficient α_i can then be obtained by fitting Eq. (3) against the results in Fig. 2(d). As expected, α is almost independent of l .

Force vs. rotation curves for the deployment are shown in Fig. 2(f). The square length $L_s = 50$ mm, the thickness $t_1 = 6$ mm, the half of cylindrical shell length is l , and the thickness is $t_2 = 0.6$ mm. a_2 and a_4 are the critical points of the snap-through instability. When the half length

of the cylindrical shell was $l = 10$ mm, then $a_2 = 0.2041$, and $a_4 = 0.29$. Moreover, the theoretical and simulation results are in good agreement. For the difference between the results from FEM and theory model, the theory model simplifies the entire structure as a rigid body, the boundary conditions are directly characterized by the rotational stiffness of the spring, and FEM considers the nonlinear deformation of the element at the boundary. Algorithm and element type of FEM will also

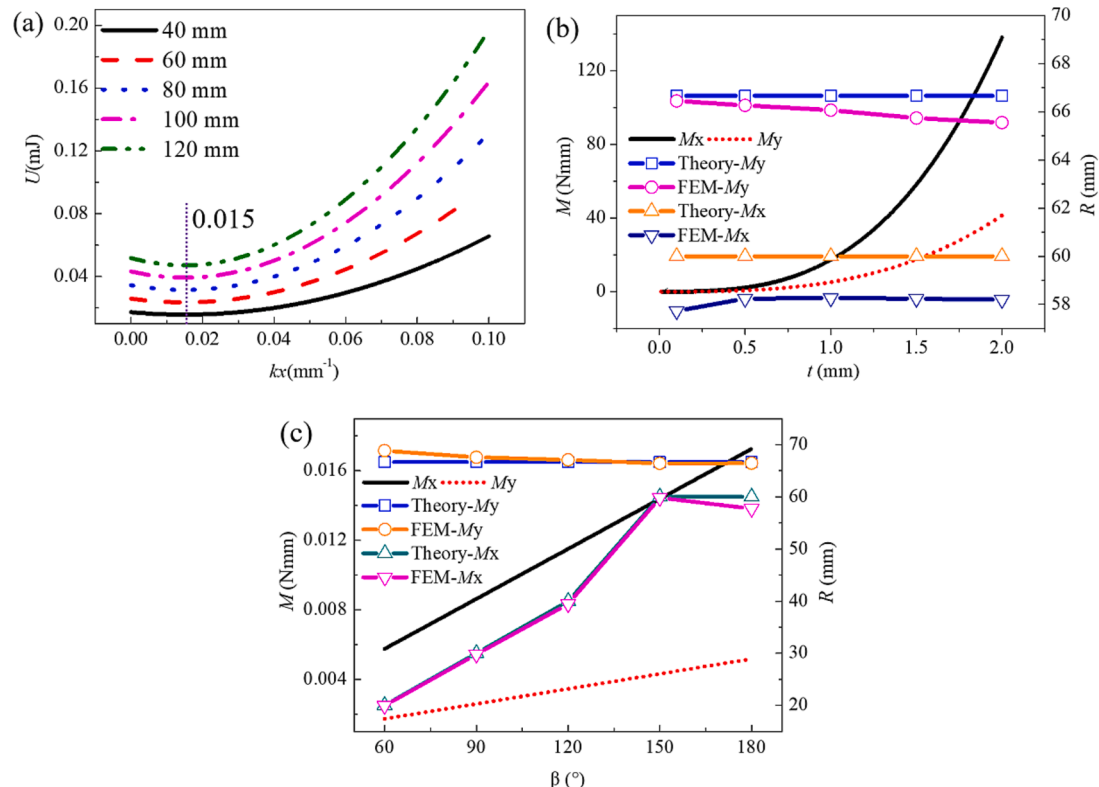


Fig. 4. (a) Total strain energy of the cylindrical shell vs. k_x for different $2l$ ($2l = 40, 60, 80, 100$, or 120 mm). Comparison of theoretical and simulation results for a cylindrical shell: (b) Moment and radius vs. thickness and (c) moment and radius of curvature vs. β .

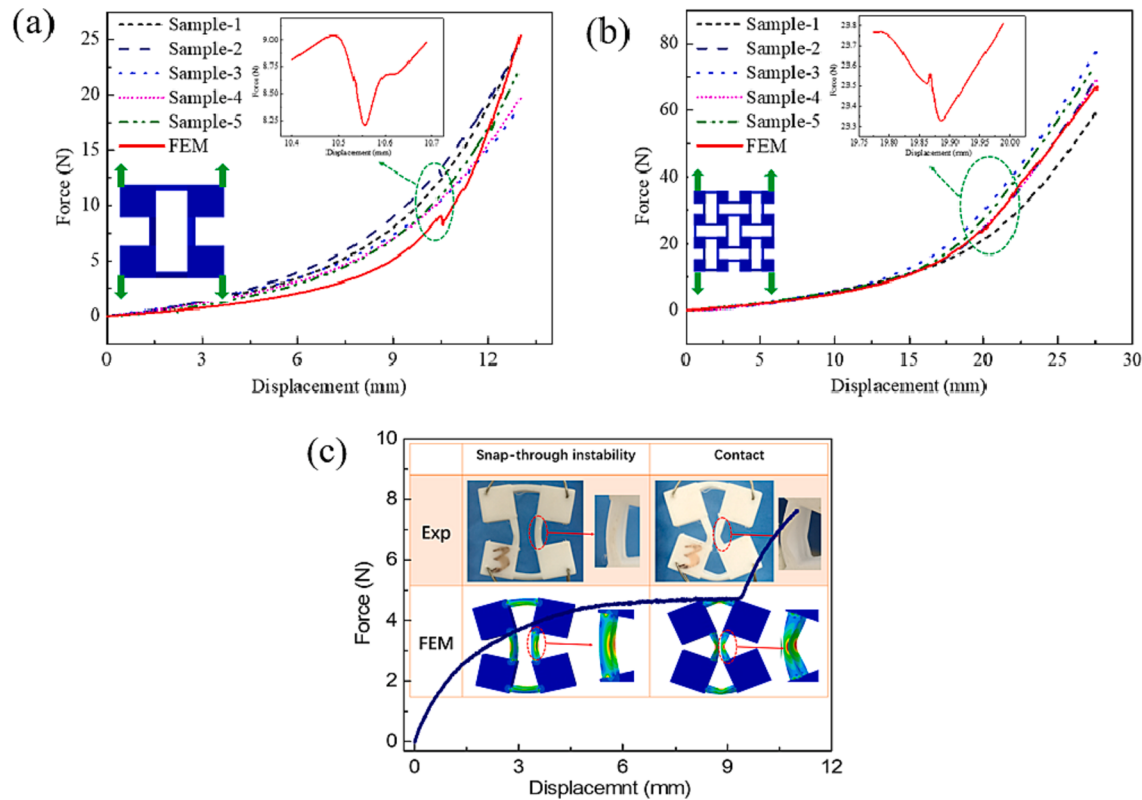


Fig. 5. (a) Applied force vs. displacement curve of a unit cell under tension. (b) Applied force vs. displacement curve of designed structure (array) under tension. (c) Applied force vs. displacement curve of the unit cell under compression.

affect the results.

4. Deployment mechanism and parametric analysis

The designed structure was fabricated by 3D printing using fused deposition modeling with a thermoplastic elastomer, polyurethane, which has excellent abrasion resistance and good elastic recovery. A stress-strain curve was obtained for the material. The material was tested experimentally to obtain the constitutive responses, which are needed as inputs for the finite element simulations. Its elastic modulus was 60 MPa, Poisson's ratio was 0.3, and density was 1200 kg/m³.

To investigate the mechanical properties of the designed structure, quasi-static tension experiments were performed with a uniaxial testing machine, as shown in Fig. 3(a). The loading rate was 1 mm/min under displacement control. The software interface was the Bluehill monitor [Fig. 3(b)], and it shows the variation of various mechanical parameters. Fig. 3(d) shows unit cells of different sizes.

By swapping only the clamping head, the testing machine can stretch or compress a specimen [Fig. 3(c)]. To analyze the evolution of the structural configuration when the specimen was stretched, the force vs. displacement curve was measured as follows. Holes were punched in the corners of the squares at the top and bottom of the designed structure [Fig. 3(e)]. Platens with holes were made from polylactic acid, and they were connected to the structure by wires. The specimen was placed at the center of the lower platen. An upward displacement load was exerted on the upper platen with a constant velocity of 5 mm/min, and the reaction force and displacement were measured [15].

A theoretical model of the bending of the cylindrical shell was established as follows. Since there is no torsion, it is assumed that the torsion curvature $k_{xy} = 0$. $2l$ is the longitudinal length of the structure. To make the cylindrical shell reach the second stable state from the initial state, either: (1) a bending moment M_y was applied to the two straight sides in the longitudinal direction to flatten the cylindrical shell

and (2) a bending moment M_x was applied to the two lateral shell sides to make the cylindrical shell bend longitudinally.

By summing the bending strain energy and tensile strain energy, the total strain energy of the cylindrical shell can be obtained as.

$$U = U_b + U_s = \frac{2\beta R_1 l}{2} \frac{Et^3}{12(1-\nu^2)} [k_x^2 + 2\nu k_x (k_y - \frac{1}{R_1}) + (k_y - \frac{1}{R_1})^2] + \frac{2lEt}{2(1-\nu^2)} \left[\frac{\beta R_1 k_x^2}{2k_y^2} + \frac{k_x^2 \sin(\beta R_1 k_y)}{2k_y^3} - \frac{4k_x^2 \sin^2(\beta R_1 k_y/2)}{\beta R_1 k_y^4} \right] \quad (4)$$

In particular, if $k_y = 0$, then $U_s = 0$. where E , ν , and t are the elastic modulus (small deformation), Poisson's ratio, and thickness, respectively. Here, R_1 is the initial cross-sectional radius of the cylindrical shell, and β is the central angle corresponding to the arc of the initial cross section.

The second steady state of the cylindrical shell corresponds to the minimum of the potential energy. In the second steady state, curvature $k_y \approx 0$. Using the principle of minimum potential energy, when the first partial derivative of the total potential energy U with respect to curvature k_x is 0, the curvature of the second steady state is.

$$\frac{dU}{dk_x} = 0 \Rightarrow k_x = \frac{D_{12}}{R_1 D_{11}} = \frac{\nu}{R_1} \quad (5)$$

The radius of curvature of the second steady state is $R_2 = 1/k_x$. Let $E = 60$ MPa, $\nu = 0.3$, $t = 0.1$ mm, $R = 20$, $2l = 40$ mm, and center angle $\beta = 180^\circ$. Next, we will discuss the variable parameters. As shown in Fig. 4(a), the influence of different lengths ($2l = 40, 60, 80, 100$, or 120 mm) on the strain energy is studied. The greater the length is, the greater the strain energy.

As shown in Fig. 4(b) and 4(c), after applying the theoretical bending moment, the theoretical radius of the deformed cylindrical shell was basically consistent with the results of the FEM for different thicknesses and values of β . As the thickness increased, the bending moment of

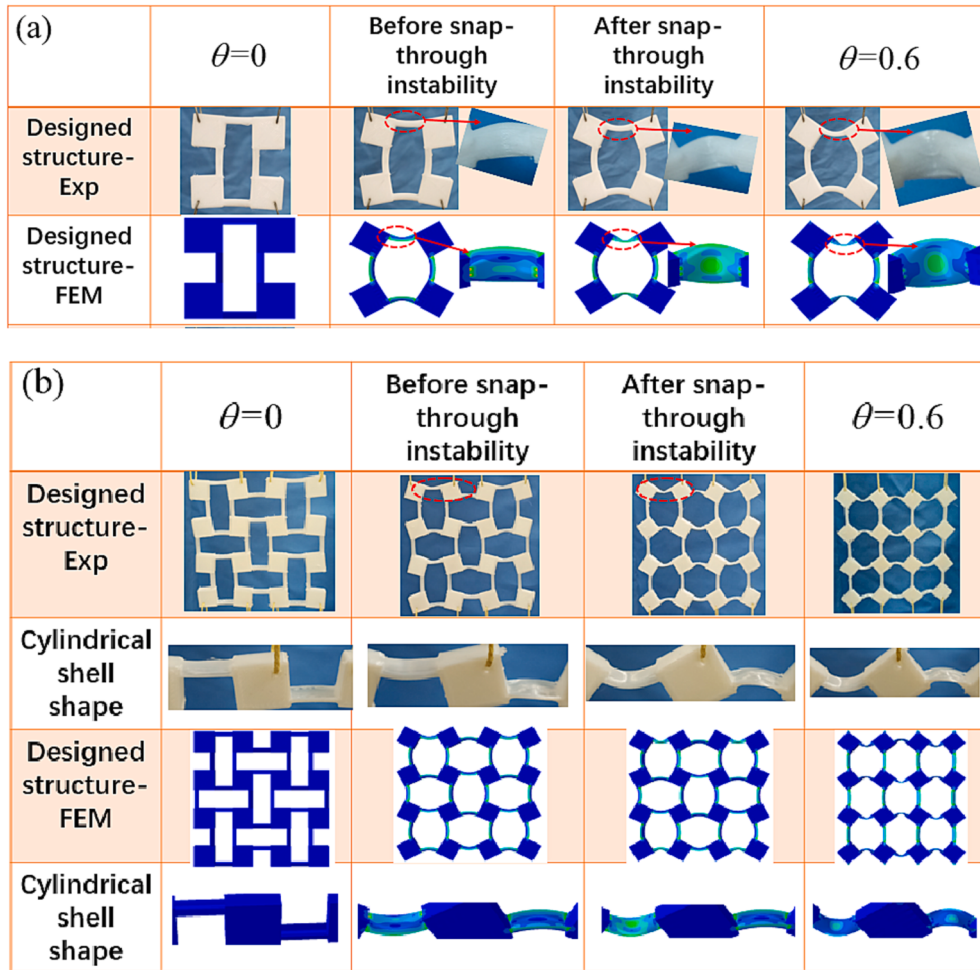


Fig. 6. Morphological evolution for (a) unit cell and (b) the designed structure.

deployment gradually increased and the strain energy gradually increased. With an increase of β , the bending moment of deployment increased linearly. The difference is mainly due to the fact that FEM considers the nonlinear deformation of the element at the boundary.

Where and how the designed structure stretches depend on the position of the applied force. When the lower part is stretched, the snap-through instability is obvious. When the upper part is stretched, the snap-through instability occurs within a small displacement.

A unit cell (5 test pieces) was stretched, and the force vs. displacement curve was measured, as shown in Fig. 5(a). The total length $L_T =$

43 mm, the thickness $t_s = 6$ mm, the length of a square was 15 mm, the cylindrical shell length $2l = 13$ mm, and the thickness $t = 0.6$ mm. As the external force increased, the structure gradually deployed. At a certain deployment position, the snap-through instability occurred (green ellipse). Initially after the instability, less energy was required to make the structure bend.

Fig. 5(b) shows the force vs. displacement curve during stretching of the structure (5 test pieces). It has the same snap-through performance as the unit cell, and the trends for the force vs. displacement curves of the two are basically the same. As the displacement increased, the

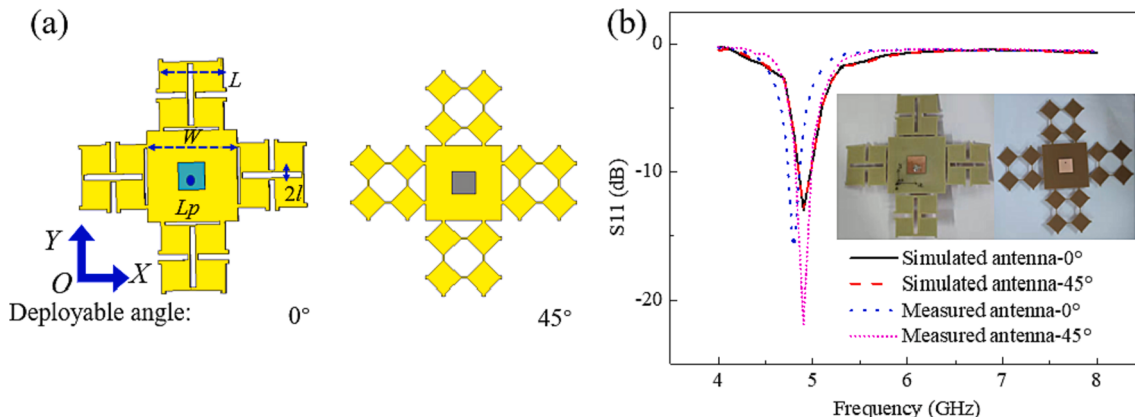


Fig. 7. (a) Designed antenna at two deployment angles [34]. (b) Reflection coefficient vs. frequency of the antenna for different deployment angles.

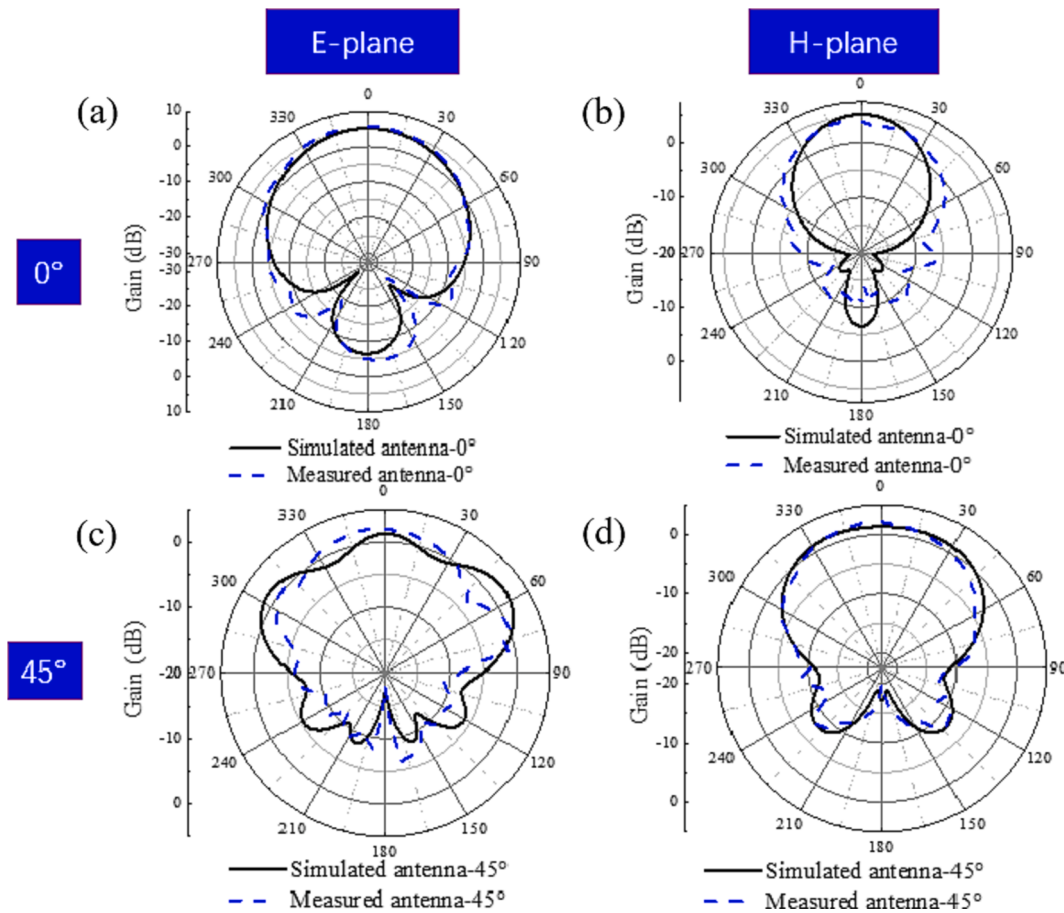


Fig. 8. Antenna gain patterns: (a) E-plane with a deployment angle of 0° . (b) H-plane with a deployment angle of 0° . (c) E-plane with a deployment angle of 45° . (d) H-plane with a deployment angle of 45° .

external load gradually increased. When the critical force was reached, the curved shell underwent the snap-through instability (green ellipse).

The force vs. displacement curve of the unit cell under compression is shown in Fig. 5(c). The force gradually increased in the early stage of compression. When the two vertical shells came into contact, the force increased linearly.

Fig. 6(a) shows the configuration of a unit cell for different tensile loads. As the structure gradually deployed, it gradually reached the critical point for the snap-through instability. Before the snap-through instability, the model deployed mainly through the rotation of each square plate. After the snap-through instability, the model deployed mainly through the stretching of the left and right cylindrical shells.

Fig. 6(b) is the morphological evolution for the designed structure. When a certain displacement was reached, the curved shell underwent the snap-through instability. The designed structure also has the same snap-through instability as the unit cell, and the trends for their force vs. displacement curves are basically the same. As the displacement increased, the external force gradually increased.

5. The illustrative application to stretchable microstrip antenna

A stretchable microstrip antenna was made with metasurfaces fabricated using the approach described above. The electromagnetic properties of the metasurfaces during the deployment process were studied with the method of moment (MoM). Mechanical drive or smart (shape memory polymer) drive method are used to realize the reconfigurable/deformation function for the designed antenna. The essence of MoM is to transform a functional equation into a matrix equation, which is solved by matrix inversion or other methods for solving linear equa-

tions. The linear vector space sum operator is expressed as $L(f) = g$, where L is the differential or integral operator, f is the field or response, and g is the source or incentive. In MoM, the continuous equations are discretized into algebraic equations, and numerical methods are used to find approximate solutions.

The designed microstrip antenna is shown in Fig. 7(a). The dielectric constant of the substrate, which was made from FR-4 epoxy glass cloth, was 4.58, the loss factor was 0.022, the side length $w = 46.56$ mm, the thickness was 1 mm, the copper thickness was 35 μm , and the overall size of the antenna was 80 mm \times 80 mm. The length of the long side of the radiation patch was 14 mm, and the length of the short side was 13.8 mm. The length of the unit cell $L = 33$ mm, and the length of the cylindrical shell $2l = 3$ mm. The feed mode used was the bottom of the coaxial line. The feeding point was 3.8 mm away from the edge of the patch. The back of the antenna was a pure metal floor with a side length of 24 mm. The reason for retaining a part of the original metal floor in the center was to facilitate the feeding of the antenna.

As shown in Fig. 7(b), the reflection coefficient S_{11} of the antenna in the 4.0–8.0 GHz band was measured in a microwave anechoic chamber with a vector network analyzer (N5227A, Agilent Technologies). At 4.90 GHz, the transmission coefficient was less than -10 dB and S_{11} was a minimum, and this was the center frequency of the radiation.

The gain patterns of the antenna for the E-plane (YOX) and H-plane (XOY) were measured, as shown in Fig. 8. As the antenna was deployed from 0° to 45° , the magnitude of the main lobe of the E-plane changed from 5.19 to 2.12 dB, and the angular width (3 dB) changed from 79.2° to 49.5° , narrowing to 29.7° . The magnitude of the main lobe of the H-plane (cross-polarization) changed from 5.19 to 1.37 dB, and the angular width (3 dB) changed from 54.9° to 106.6° , which is an increase

of 51.7°. This shows that the electromagnetic energy radiated by the antenna diverged, so that the gain fell during the deployment.

6. Conclusions

This paper presents a structure fabricated with square plates and cylindrical shells. The following conclusions are drawn:

(1) A mechanical spring model was established to study the deployment of the designed structure. The elastic deformation energy stored in the mechanical system was calculated, and the applied force was derived from the displacement. The mechanical characteristics of the structure were obtained and the accuracy was verified through experiments and FEM. The snap-through curve of the structure is a non-linear superposition of the two cylindrical shells. If the length, thickness, etc. of the cylindrical shell are reasonable, then snap-through can be realized at any angle.

(2) The deployment mechanism and parameterization of the structure were analyzed. The snap-through characteristics of the cylindrical shell were analyzed, and the deployment of the designed structure was studied. Experiments and simulations were used to explore the configuration and calculate the force vs. displacement curve of the designed structure. Initially after the instability, less energy was required to make the bend. The structure has a high bending stiffness, which is good for shape retention. The section moment of inertia of the designed structure was significantly increased, which may be useful for aerospace applications.

(3) A stretchable microstrip antenna was designed to achieve high gain for the same center frequency for different deployment angles. With the gradual deployment of the system, the tensile elongation of the antenna was 17.8% but the center frequency did not change much. The measured and simulated results are in good agreement. The electromagnetic energy radiated by the antenna diverged, so that the gain reduced after the deployment.

This analysis of the deployment of a flexible kirigami structure may provide guidance for the application of deformable structures.

CRediT authorship contribution statement

Ji Zhang: Conceptualization, Methodology, Software, Validation, Formal analysis, Investigation, Resources, Data curation, Writing – original draft, Writing – review & editing, Visualization. **Lamei Zhang:** Investigation, Validation, Writing – review & editing. **Yafei Wang:** Investigation, Supervision, Writing – review & editing. **Youshan Wang:** Supervision, Writing – review & editing. **Changguo Wang:** Conceptualization, Supervision, Writing – review & editing, Visualization, Project administration, Funding acquisition.

Declaration of Competing Interest

The authors declare that they have no known competing financial interests or personal relationships that could have appeared to influence the work reported in this paper.

Acknowledgment

The authors gratefully acknowledge financial support from the National Natural Science Foundation of China (grant 11872160,12172102) and the Science Foundation of the National Key Laboratory of Science and Technology on Advanced Composites in Special Environments (grant JCKYS2020603C007). The authors would like to thank Dr. Shu Lin from Harbin Institute of Technology in Harbin, China, for his invaluable contributions in measuring the electrical properties of the antenna.

References

- [1] Zhang Y, Yan Z, Nan K, Xiao D, Liu Y. A mechanically driven form of kirigami as a route to 3D mesostructures in micro/nanomembranes. *Proc Natl Acad Sci* 2015;112(38):11757.
- [2] Wang F, Guo X, Xu J, Zhang Y, Chen C. Patterning curved three-dimensional structures with programmable kirigami designs. *ASME J Appl Mech* 2017;84(6):061007.
- [3] Choi G, Dudte L, Mahadevan L. Programming shape using kirigami tessellations. *Nat Mater* 2019;18:999–1004.
- [4] Neville RM, Monti A, Hazra K, Scarpa F, Remillat C, Farrow IR. Transverse stiffness and strength of Kirigami zero-v PEEK honeycombs. *Compos Struct* 2014;114:30–40.
- [5] Shi X, Xu R, Li Y, Zhang Y, Ren Z, Gu J, et al. Mechanics design for stretchable, high areal coverage gaAs solar module on an ultrathin substrate. *ASME Appl Mech* 2014;81(12):124502.
- [6] Celli P, Lamaro A, McMahan C, Bordeennithikasem P, Hofmann D, Daraio C. Compliant morphing structures from twisted bulk metallic glass ribbons. *J Mech Phys Solids* 2020;145:104129.
- [7] Du YT, Keller T, Song CP, Wu LZ, Xiong J. Origami-inspired carbon fiber-reinforced composite sandwich materials – Fabrication and mechanical behavior. *Compos Sci Technol* 2021;205:108667.
- [8] Lamoureux A, Lee K, Shlian M, Forrest SR, Shtein M. Dynamic kirigami structures for integrated solar tracking. *Nat Commun* 2015;6:8092.
- [9] Armanini C, Dal Corso F, Misseroni D, Bigoni D. Configurational forces and nonlinear structural dynamics. *J Mech Phys Solids* 2019;130:82–100.
- [10] Cazzolli A, Misseroni D, Dal Corso F. Elastica catastrophe machine: theory, design and experiments. *J Mech Phys Solids* 2020;136:103735.
- [11] Ma JY, Song JC, Chen Y. An origami-inspired structure with graded stiffness. *Int J Mech Sci* 2018;136:134–42.
- [12] Lyu SN, Qin B, Deng HC, Ding XL. Origami-based cellular mechanical metamaterials with tunable Poisson's ratio: Construction and analysis. *Int J Mech Sci* 2021;212:106791.
- [13] Zhang J, Li T, Wang C, Yan X. Aerodynamic drag characteristics of Miura-ori composite structure. *J Aerospace Eng* 2021;34(4):06021004.
- [14] Zhang J, Wang C, Guo J, Zhang JW. Pressure-induced instability and its coupled aeroelasticity of inflated pillow. *Chin J Aeronaut* 2021;35(2):1–7.
- [15] Tang Y, Li Y, Hong Y, Yang S, Yin J. Programmable active kirigami metasheets with more freedom of actuation. *Proc Natl Acad Sci* 2019;116:26407–13.
- [16] Wang ZJ, Jing LQ, Yao K, Yang YH, Zheng B, Soukoulis CM, et al. Origami-based reconfigurable metamaterials for tunable chirality. *Adv Mater* 2017;29(27):1700412.
- [17] Rodrigues VG, Fonseca ML, Savi AM, Paiva A. Nonlinear dynamics of an adaptive origami-stent system. *Int J Mech Sci* 2017;133:303–18.
- [18] Li Y, Pellegrino S. A theory for the design of multi-stable morphing structures. *J Mech Phys Solids* 2020;136:103772.
- [19] Feng F, Dang XX, James RD, Plucinsky P. The designs and deformations of rigidly and flat-foldable quadrilateral mesh origami. *J Mech Phys Solids* 2020;142:104018.
- [20] Meng ZQ, Liu MC, Zhang YF, Chen CQ. Multi-step deformation mechanical metamaterials. *J Mech Phys Solids* 2020;144:104095.
- [21] Chen Y, Ma Y, Yin Q, Pan F, Cui C, Zhang Z, et al. Advances in mechanics of hierarchical composite materials. *Compos Sci Technol* 2021;214:108970.
- [22] Meng ZQ, Chen WT, Mei T, Lai YC, Li YX, Chen CQ. Bistability-based foldable origami mechanical logic gates. *Extreme Mech Lett* 2021;43:101180.
- [23] Del Broccolo S, Laurennzi S, Scarpa F. AUXHEX – A Kirigami inspired zero Poisson's ratio cellular structure. *Compos Struct* 2017;176:433–41.
- [24] Lele A, Deshpande V, Myers O, Li SY. Snap-through and stiffness adaptation of a multi-stable kirigami composite module. *Compos Sci Technol* 2019;182:107750.
- [25] Kebadze E, Guest SD, Pellegrino S. Bistable prestressed shell structures. *Int J Solids Struct* 2004;41(11–12):2801–20.
- [26] Son D, Hyun J, Lee J. Prediction and validation of electromagnetic performance of curved radar-absorbing structures based on equivalent circuit model and ray tracking method. *Compos Sci Technol* 2018;167:547–54.
- [27] Li Y, Chandra A, Dorn CJ, Lang RJ. Reconfigurable surfaces employing linear-rotational and bistable-translational (lrbt) joints. *Int J Solids Struct* 2020;207:22–41.
- [28] Cazzolli A, Dal Corso F. Snapping of elastic strips with controlled ends. *Int J Solids Struct* 2019;162:285–303.
- [29] Zhang Z, Ma WL, Wu HL, Wu HP, Jiang SF, Chai GZ. A rigid thick Miura-ori structure driven by bistable carbon fibre-reinforced polymer cylindrical shell. *Compos Sci Technol* 2018;167:411–20.
- [30] Zhao P, Wang YX, Katz B, Mockensturm E, Crespi V, Zhang SL. Geometry and chiral symmetry breaking of ripple junctions in 2D materials. *J Mech Phys Solids* 2019;131:337–43.
- [31] Bae H, Bae S, Yoon J, Park C, Kim K, Kwon S, et al. Self-organization of maze-like structures via guided wrinkling. *Sci Adv* 2017;3(6):e1700071.
- [32] Zhang J, Wang CG, Zhang LM. Deployment of SMP Miura-ori sheet and its application: aerodynamic drag and RCS reduction. *Chin J Aeronaut* 2021.
- [33] Zhang J, Liu S, Zhang LM, Wang CG. Origami-based metasurfaces: design and radar cross section reduction. *AIAA J* 2020;58(5):5478–82.
- [34] Zhang J, Miao WX, Zhang LM, Wang CG. Kirigami-based stretchable low-radar-cross-section microstrip antenna: Design and Analysis. *AIAA J* 2022;60(3):1958–64.
- [35] Zheludev NI. The road ahead for metamaterials. *Science* 2010;328:582–3.

- [36] Zhang M, Yang J, Zhu R. Origami-based bistable metastructures for low-frequency vibration control. ASME J Appl Mech 2021;88(5):051009.
- [37] Maguid E, Yulevich I, Veksler D, Kleiner V, Brongersma M, Hasman E. Photonic spin-controlled multifunctional shared-aperture antenna array. Science 2016;352(6290):1202–6.
- [38] Tang YC, Lin GJ, Han L, Qiu SG, Yang S, Yin J. Design of hierarchically cut hinges for highly stretchable and reconfigurable metamaterials with enhanced strength. Adv Mater 2015;27(44):7181–90.
- [39] Xiang Y, Zhong D, Rudykh S, Zhou H, Qu S, Yang W. A review of physically based and thermodynamically based constitutive models for soft materials. ASME J Appl Mech 2020;87(11):110801.
- [40] Blees M, Barnard A, Rose P, Roberts S, McGill K, Huang P, et al. Graphene kirigami. Nature 2015;524:204–7.
- [41] Xie Z, Ji B, Huo Q. Mechanics design of stretchable near field communication antenna with serpentine wires. ASME J Appl Mech 2018;85(4):045001.
- [42] An N, Domel AG, Zhou J, Rafsanjani A, Bertoldi K. Programmable Hierarchical Kirigami. Adv Funct Mater 2020;1906711.